

Lignin-Derived Functional Carbon Framework for Homogeneous Sodium Deposition

Xiwei Li,^[a] Yi Qi,^[a] Xuliang Lin,^[a, b, d] Xianhong Rui,^{*[c]} and Yanlin Qin^{*[a, b, d]}

Sodium metal batteries have become popular owing to their low redox potential, high theoretical capacity, and superior energy density. But the formation of sodium dendrites during electrochemical cycles diminishes the security and longevity of these batteries. In response to this challenge, we employ lignin as a carbon source to fabricate a three-dimensional (3D) carbon framework current collector. This framework boosts an expansive specific surface area and a wealth of oxygen-rich functional groups. These components serve to cushion the volume fluctuations of sodium metal throughout the electrochemical

cycle, directing the even deposition of sodium ions. The as-prepared anode displays a low overpotential of -7 mV and a stable cycling life of 400 hours at 0.5 mA cm^{-2} . When coupled with $\text{Na}_3\text{V}_2(\text{PO}_4)_3$ cathode, the full cell can achieve a capacity of 97.6 mAh g^{-1} and a capacity retention of 94.7% after 60 cycles. This research shows that using lignin as a carbon source to prepare a 3D carbon framework current collector is an effective mean to inhibit the harmful effects of sodium dendrites on batteries.

1. Introduction

Over the past three decades, lithium-ion batteries (LIBs) have consistently represented the leading technology in the energy storage market. With the development of renewable energy sources, the pursuit of efficient, cost-effective, and safe energy storage technologies has become imperative. However, lithium metal resources are not unlimited, and the cost issue has yet to be resolved. These issues are forcing researchers to explore next-generation energy storage technologies beyond LIBs.^[1-3] To this end, sodium-ion batteries (SIBs) stand out by view of comparable physical and chemical characteristics of metallic Na compared to Li.^[4,5] Among the diverse anode materials for SIBs, the sodium metal anode stands apart with a notable theoretical capacity of 1166 mAh g^{-1} , coupled with lower redox potential compared to other materials, and cost-effectiveness.^[6] Unfortunately, the uncontrollable hazards of sodium dendrites at the electrode/electrolyte boundary significantly restricts its practical development.^[7-10] Furthermore, side reactions occurring at the boundary between sodium metal and electrolyte compromise the stable coulombic efficiency of SIBs, leading to the

generation of the notorious “dead Na”. Therefore, addressing how to eliminate the impact of the aforementioned unfavorable conditions is a pressing issue for the application of sodium metal batteries (SMBs).^[11]

To constrain the hazards of sodium dendrites, current common strategies involve optimizing the electrolyte composition, designing a three-dimensional (3D) conductive current collector and an artificial solid electrolyte interphase (SEI) cover on the anode surface.^[12,13] However, most research in electrolyte optimization tends to impede the Na^+ diffusion in the electrolyte. Electrode/electrolyte interfaces form a thick SEI layer as a result, leading to a significant polarization voltage.^[14,15] Moreover, the construction of artificial SEI often leads to insufficient interfacial contacts.^[16] On the contrary, 3D conductive current collector featuring large active area, sufficient contact with electrolyte and controllable deposition morphology of Na^+ have attracted widespread attention.^[17] These unique features empower it to facilitate highly reversible Na deposition/stripping with a low polarization voltage.^[18] Thus, developing 3D current collector is an effective approach to constructing high-performance SMBs.^[19,20]

The role of 3D current collector primarily serves a dual purpose. Firstly, it provides a buffer space for the large volume changes of Na metal.^[21] Secondly, by adjusting the reaction conditions to achieve the optimal specific surface area size, the 3D current collector can play a role in reducing local current and providing sodophilic sites.^[22,23] According to different types of synthetic raw materials, 3D current collector can be broadly categorized into three groups. (1) 3D carbon-based framework (3D CBF) with carbon as raw material. Nitrogen–oxygen codoped graphitized carbon fibers (DGCF) were developed as the matrix for Na plating, Na metal nucleates uniformly under its guidance, and dendrite growth is inhibited.^[24] (2) Using 3D metal-base framework (3D MBF) as raw material. For example, a Cu foam skeleton with layered ZnO nanorods array (CF@ZnO) was synthesized as a robust substrate for Na metal anodes.^[25]

[a] X. Li, Y. Qi, X. Lin, Y. Qin

School of Chemical Engineering and Light Industry, Guangdong University of Technology, Guangzhou, Guangdong 510006, PR China
E-mail: ylqin@gdut.edu.cn

[b] X. Lin, Y. Qin

Provincial Key Laboratory of Plant Resources Biorefinery, Guangdong University of Technology, Guangzhou, 510006, China

[c] X. Rui

School of Materials and Energy, Guangdong University of Technology, Guangzhou, 510006, China
E-mail: xhrui@gdut.edu.cn

[d] X. Lin, Y. Qin

Jieyang Branch of Chemistry and Chemical Engineering Guangdong Laboratory, Jieyang 515200, PR China

 Supporting information for this article is available on the WWW under <https://doi.org/10.1002/batt.202400050>

(3) 3D composite framework (3D CF) using composites as raw materials. For example, Fang et al. prepared metal clusters anchored on the N-doped carbon nanotube frameworks (CC@Co-NCNTs and CC@Fe-NCNTs) based on the findings from first-principles calculations. They demonstrated that these metal clusters also contribute to Na affinity.^[26] Among various preparation materials, carbon materials stand out due to their ease of preparation, cost-effectiveness and wide availability. This leads to extensive research on 3D CBF. Out of all the carbon sources, industrial lignin is obtained from the by-product of pulping and papermaking processes. It possesses abundant oxygen-containing functional groups that can function as sites favorable for sodium deposition, ensuring uniformity. The utilization of lignin as a biomass-derived carbon materials in the creation of 3D CBF holds great possible applications across diverse contexts.

In this investigation, we synthesized a porous carbon skeleton called LFC (Lignin Flower Carbon) combining lignin calcination and a template agent through a simple template method. LFC was designed to serve as the host of SMB. Benefiting from the group and structure of lignin, the LFC material possesses oxygen functional groups that exhibit sodium affinity, along with a large surface area. These features contribute for achieving uniform deposition of sodium and preventing sodium dendritic crystal growth during the electrochemical cycle. LFC sodium anodes have a nucleation over-

potential of -7 mV and a coulombic efficiency (CE) of 99.41%. Additionally, we set the surface capacity at 2 mAh cm^{-2} , the symmetric battery of LFC-Na exhibits stable cycling for 400 hours at 0.5 mA cm^{-2} . The LFC Na | Na₃V₂(PO₄)₃ full battery showed demonstrated a performance 97.6 mAh g^{-1} after 60 cycles. This study highlights the potentiality of LFC materials as negative electrode materials for SMBs and provides valuable insight into their electrochemical properties.

2. Results and Discussion

The synthesis diagram of LFC-Na is shown in Figure 1a. This study adopts a template method to prepare carbon materials. In brief, the alkali lignin and magnesium oxide template agent were mixed and stirred in water at room temperature. The solution was heated until it reached a boiling point, which was then transferred into a tube furnace for high-temperature calcination to obtain porous carbon framework. Subsequently, an electrochemical deposition process was utilized to deposit Na onto the carbon framework. The images below show the results of scanning electron microscopy (SEM) (Figures 1b, c, d), the LFC matrix maintained porous structure due to the removal of the template agent MgO. X-ray diffraction (XRD) patterns (Figure 1d) display a broaden diffraction peak at $\sim 18^\circ$ for LPC. The SEM and XRD results collectively indicate the porous

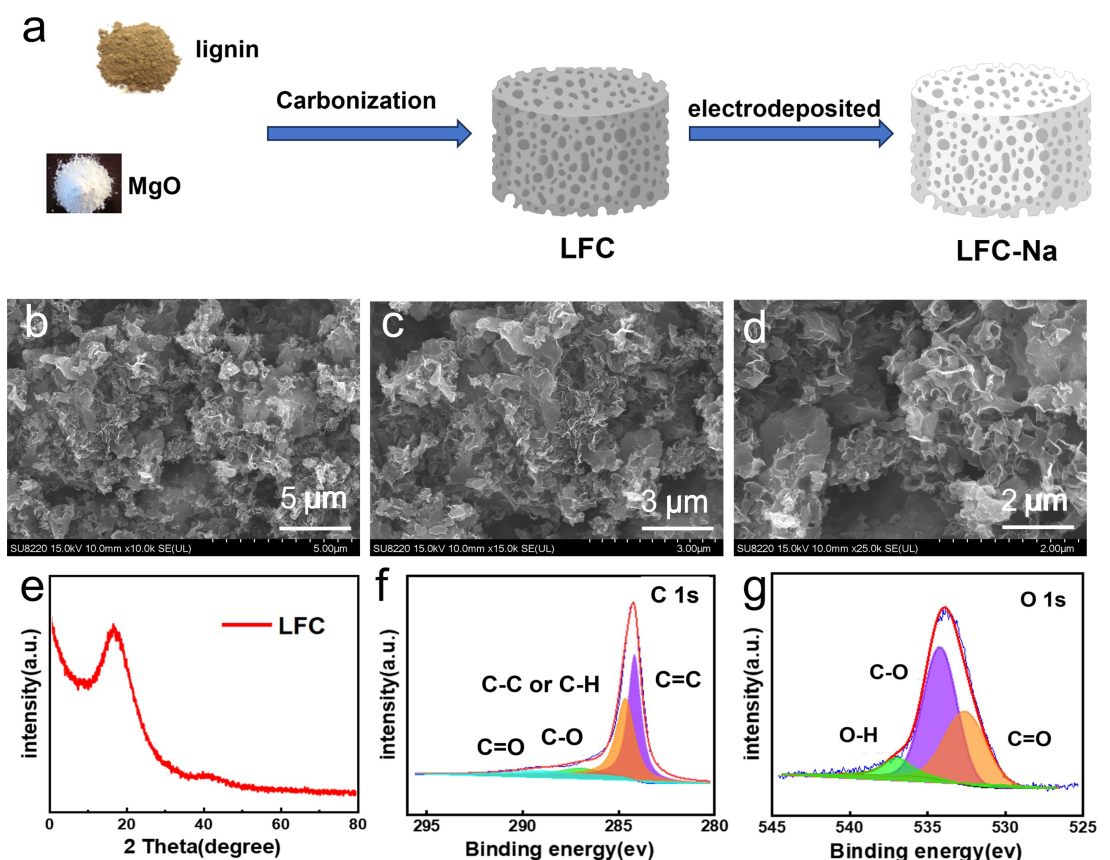


Figure 1. (a) Schematic diagram of the preparation steps of LFC. (b,c,d) SEM images and (e) X-ray diffraction pattern of LFC. High-resolution XPS spectra of (f) C1s, and (g) O1s of the LFC.

structure of the LFC material, with effective removal of the residual template agent through washing. The crystallization degree of carbon in LFC was analyzed through the Raman spectra (Figure S1). Raman spectra show the characteristics of D- and G-band at 1328 cm^{-1} , and 1527 cm^{-1} , respectively. The emergence of the G band stems from the porous structure within the carbon material, while the D band rises with increasing levels of graphitization. The intensity ratio of D-band and G-band (I_D/I_G) is calculated to be 0.92, indicative of partial graphitization in LFC. According to the literature report, the partial graphitization of carbon is beneficial to electron transport.^[27,28] To investigate the elemental composition and forms within LFC, X-ray photoelectron spectroscopy (XPS) was used to test the system. (Figure 2). The C1s spectrum of LFC can be fitted into four peaks, with the major peaks being C=C (283.6 eV) and C-C or C-H (284.4 eV), and the two minor peaks being C-O (533.0 eV) and C=O (531.6 eV). As lignin is a three-dimensional biopolymer formed by the connection of three phenylpropane units through ether and carbon–carbon bonds, it possesses a network structure rich in aromatic rings, aliphatic and aromatic hydroxyl groups, as well as quinone functional groups. This abundance of functional groups in lignin-derived carbon materials sets them apart from conventional commercial carbon materials. In the O 1s spectrum of LFC, three peaks can also be fitted into C-O (533.0 eV), C=O (531.6 eV), and O-H (535.6 eV). The peak intensity of C-O further substantiates the presence of unique functional group structures in carbon materials derived from lignin, serving as evidence for its distinct composition. XPS tests were also conducted on carbon black and carbon spheres for comparison (Figure S3). Compared to carbon black, LFC, derived from an alkali lignin carbon source, imparts sodium-friendly oxygen-containing functional groups. These features facilitate the uniform deposition of sodium during the electrochemical cycle.^[29] Furthermore, the surface area of LFC, carbon spheres and carbon black were determined

through the analysis of nitrogen adsorption and desorption isotherms (Figures S2 and S4). The surface area of LFC is $749.2\text{ m}^2/\text{g}$, compared to carbon black ($215.9\text{ m}^2/\text{g}$) and carbon spheres ($1.3\text{ m}^2/\text{g}$), LFC has a much higher surface area. Large specific surfaces can mitigate local currents in 3D current collectors.^[30] The affinity groups in LFC also provide a significant advantage by preventing Na dendrite formation.^[31–33]

To validate the aforementioned points, the produced LFC–Na was characterized using SEM and EDS. A current density of 0.5 mA cm^{-2} and a plating capacity of 2 mAh cm^{-2} were used in the test. Figure 2a shows that the deposition of sodium on LFC is uniform and dense, occupying the pores inside LFC. The EDS mapping results show dense and uniform Na coverage. Moreover, the cross-section morphology (Figure 2b) reveals that the deposited sodium infiltrates the pore structure of LFC rather than remaining on the surface. These findings suggest that the LFC material maintains a stable structure throughout the electrochemical process, and its morphological design contributes to preventing the growth of sodium dendrite.^[34–36]

To evaluate reversibility, we formulated a slurry by combining LFC with a binder. The slurry was then coated onto aluminum foil and assembled with metallic sodium to create a half-cell (LFC || Na), allowing us to test its CE, a critical criterion for evaluating deposition/stripping. In this examination, we conducted tests at current densities of 0.5 mA cm^{-2} and 1.0 mA cm^{-2} , with a specific capacity of 2 mAh cm^{-2} . The charging cut-off voltage was set at 0.5 V. Two electrolytes, namely 1 M sodium hexafluorophosphate dissolved in tetrahydrofuran (THF) and 1 M sodium hexafluorophosphate dissolved in ethylene glycol dimethyl ether (DME), were simultaneously employed (Figure 3). Set the current density to 0.5 mA cm^{-2} , the CE curves of LFC || Na cells using both electrolytes show stable performance (Figures 3a, c). The current density increases to 1 mA cm^{-2} when the density is increased, the LFC || Na cell using the THF electrolyte becomes more stable. While in the

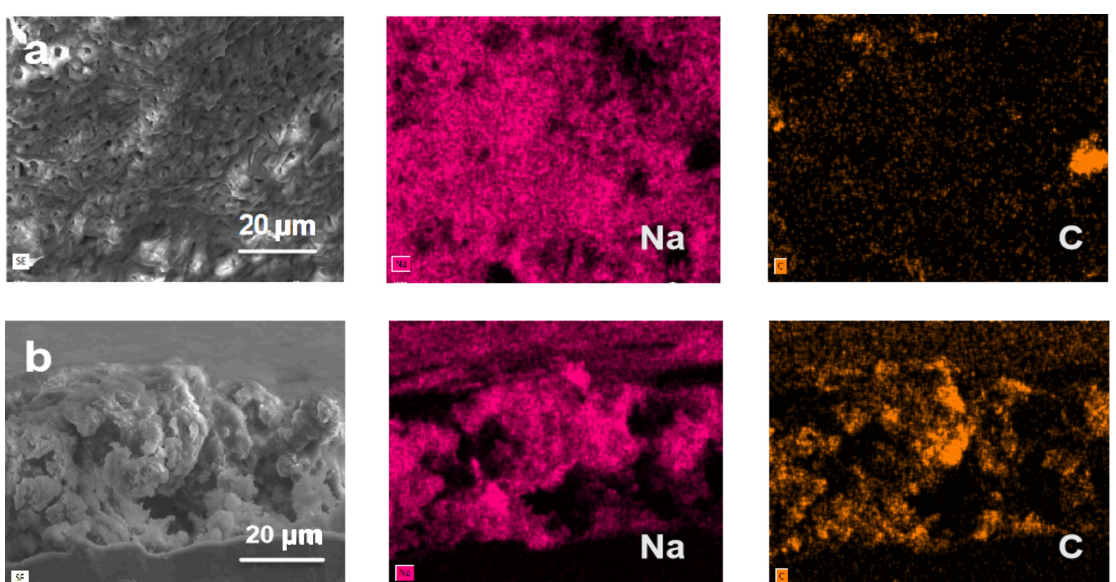


Figure 2. (a,b)SEM morphologies and elemental mapping images of the LFC–Na. The scale bars are $20\text{ }\mu\text{m}$.

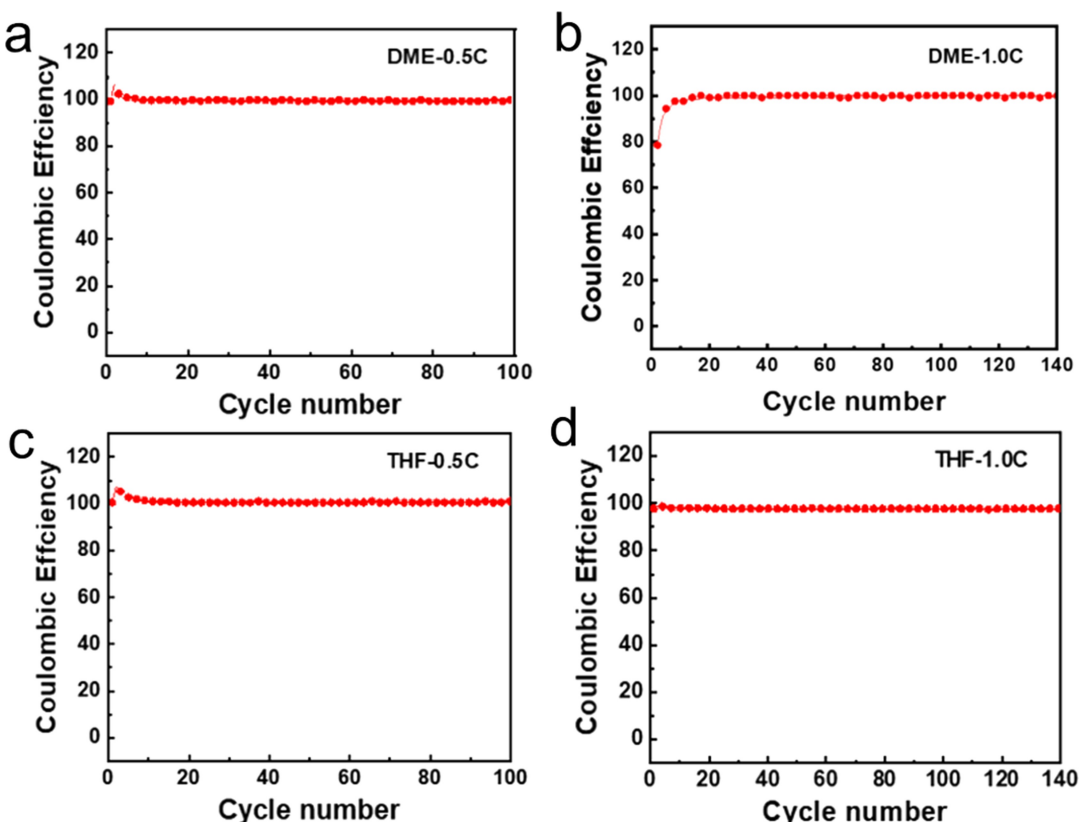


Figure 3. CE curves of LFC || Na cells using (a–b) DME and (c–d) THF electrolytes at current densities of (a, c) 0.5 mA cm^{-2} and (b, d) 1.0 mA cm^{-2} .

DME electrolyte, the initial CE of the cell is 78.52% (Figure 3b). According to the present study, THF's weak ion solvation and desolvation greatly promotes rapid ion diffusion when it is in contact with an electrolyte. Simultaneously, the uniform distribution of NaF and organic components in the electrolyte stabilizes the SEI layer and promotes rapid Na^+ diffusion.^[37] Moreover, the porous structure of LFC allows for smooth electrolyte penetration, shortening the diffusion path.^[38,39]

We conducted a test to observe the electroplating behavior of metal Na at 0.5 mA cm^{-2} , simultaneously comparing the characteristics of LFC, carbon black (SP), and carbon sphere (CS) (Figure 4a). Results indicated that the nucleation overpotential of LFC (-7 mV) was lower than that of SP (-18 mV) and CS (-17.6 mV). This phenomenon may arise from the selective nucleation of Na at sodiophilic sites induced by the larger specific surface area and richer functional groups of LFC materials. Previous studies have suggested that a lower nucleation overpotential is beneficial for achieving uniform Na deposition and minimizing the risk of sodium dendrite formation.^[36,40,41] Furthermore, the overpotential of Na nucleation in LFC was examined across a spectrum of current densities, spanning from 0.5 to 2 mA cm^{-2} (Figure 4b). Clearly, the overpotential exhibited a gradual and steady increase, affirming that LFC had a positive impact on Na nucleation at different current densities.^[42] A transparent quartz half-cell was assembled for in-situ optical observation of Na dendrite growth. In this half-cell, the negative electrode is comprised of an

electrode sheet and terminal tabs. The half-cell was discharged at a constant current density of 0.5 mA cm^{-2} for one hour (Figure 4c, d). The LFC frameworks exhibited minimal dendrite growth during the deposition process, with no observable large Na dendrites appearing as the deposition process continued. In contrast, the commercial carbon black demonstrated noticeable Na dendrites at the early stage ($t = 15 \text{ min}$). As the deposition time increased, the Na dendrites grew uncontrollably, covering nearly the entire surface. This is attributed to the relatively small specific surface area of commercial carbon materials, preventing them from effectively facilitating the uniform deposition of sodium metal during the electrochemical cycling process. In contrast, the LFC material not only possesses a larger specific surface area but also features a well-developed porous structure, enabling the LFC framework to effectively promote the uniform deposition of sodium. The in-situ optical observations confirmed that the LFC framework can effectively facilitate uniform sodium deposition.

We assembled symmetric cells with two identical LFC–Na electrodes to assess the polarization performance. In comparison, symmetric cells (SP–Na || SP–Na and CS–Na || CS–Na) were configured by the same method. The sodium metal areal capacity on the electrode is 2 mAh cm^{-2} . Cells with SP–Na || SP–Na and CS–Na || CS–Na configurations showed consistent voltage fluctuations and unstable voltage polarization occurs within a short period (Figure 5a). This may ascribe to the unstable SEI layers induced by repeated growth of Na

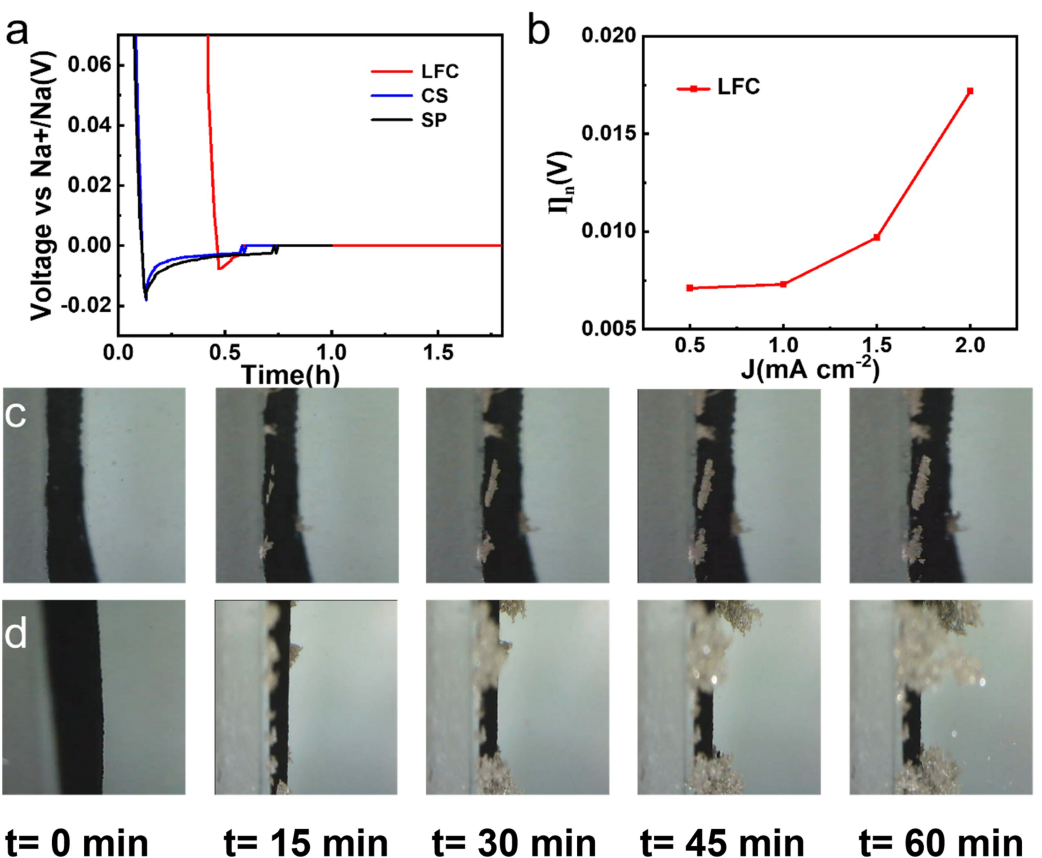


Figure 4. (a) Voltage-time curves during Na nucleation at 0.5 mA cm^{-2} on LFC, SP, and CS electrodes. (b) The Na nucleation overpotentials (η_n) of LFC at different current densities (J). (c-d) Optical images of in-situ observation of the Na plating behavior on (c) LFC and (d) SP at 0.5 mA cm^{-2} .

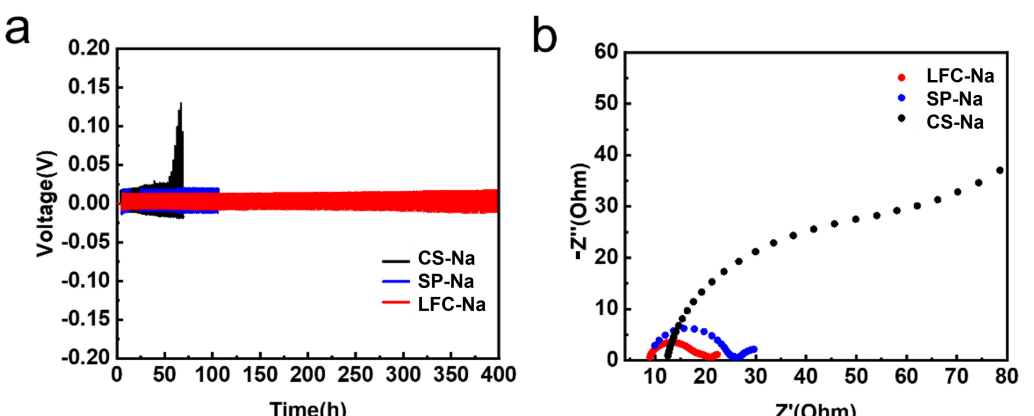


Figure 5. (a) Voltage curves over time of the symmetrical cells with LFC–Na || LFC–Na, CS–Na || CS–Na, SP–Na || SP–Na configurations at a deposition current density of 0.5 mA cm^{-2} . (b) EIS curves of the LFC–Na, CS–Na, and SP–Na symmetrical cells after 10 cycles.

dendrites.^[43] The voltage fluctuation kept intensified over time for SP–Na || SP–Na and CS–Na || CS–Na cells. After 60 hours cycling, the CS–Na || CS–Na cell experienced a sudden voltage increase, ultimately resulting in an internal short circuit. In contrast, the LFC–Na || LFC–Na cell displayed a stable voltage curve for over 400 hours. Because the LFC material facilitates more uniform sodium deposition, producing more stable SEI layers. The electrochemical impedance spectroscopy (EIS) curves of these symmetrical batteries after 10 cycles are shown

in Figure 5b. The semicircle of the impedance curve is closely related to the charge transfer resistance.^[44] After 10 cycles, the SP–Na || SP–Na and CS–Na || CS–Na cells exhibit poor polarization performance compared to LFC–Na || LFC–Na. This difference is attributed to the formation of more Na dendrites during cycling. The lower charge transfer resistance of LFC–Na (9.96 Ω vs. 20.7 Ω for SP–Na and 71.86 Ω for CS–Na) indicates the inhibition of sodium dendrite growth in the cell, leading to the formation of a uniform SEI layer conducive to Na^+ diffusion.^[45]

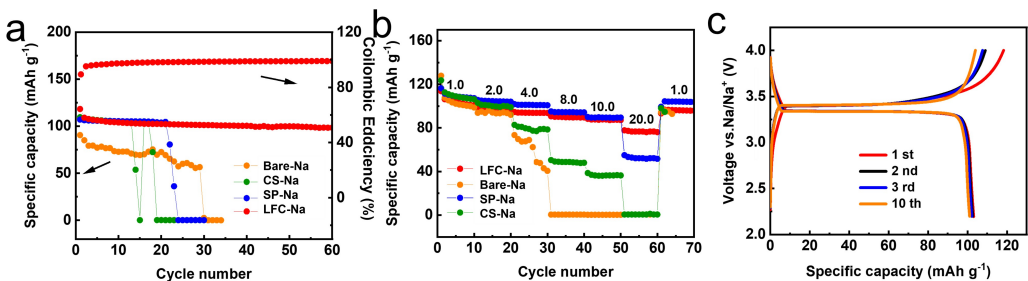


Figure 6. (a) Cycling stability of LFC–Na and bare Na, CS–Na, SP–Na || NVP full cells at a current density of 100 mA g^{-1} . (b) Rate capability of LFC–Na and bare Na, CS–Na, SP–Na//NVP. ($1 \text{ C} = 117.6 \text{ mA g}^{-1}$) (c) Charge-discharge profiles of the LFC–Na || NVP full cells at a current density of 100 mA g^{-1} .

The two contrasting samples prepared exhibit poorer polarization and larger impedance compared to LFC, attributed to the ineffective suppression of sodium dendrite growth by commercial carbon materials. This results in the generation of dendrites capable of piercing the SEI layer during electrochemical cycling, ultimately leading to a significant deterioration in battery performance.

Full cells based on the LFC–Na anode and the $\text{Na}_3\text{V}_2(\text{PO}_4)_3$ (NVP) cathode were assembled to assess the practical implementation of the composite anode. Long-term cycling behavior of the LFC–Na || NVP full cell was studied, maintaining a rate of 100 mA g^{-1} . (Figure 6a). After 60 cycles, the LFC–Na || NVP cell delivered a capacity of 97.6 mAh g^{-1} , retaining approximately 94.7% of its initial capacity, indicative of its long-term durability. In contrast, SP–Na || NVP and CS–Na || NVP showcased fast capacity decay and poor stability. While SP–Na || NVP and CS–Na || NVP initially showed reasonable capacity stability, a short circuit occurred around 20 cycles. Furthermore, a full cell based on bare sodium and NVP (bare-Na || NVP) was assembled and tested. It exhibited poor capacity attenuation and inferior stability, and experienced unstable fluctuations in early cycles, leading to a short circuit around 30 cycles. Figure 6b shows the rate capabilities of the full cells at different C-rates, ranging from 1 C to 20 C ($1 \text{ C} = 117.6 \text{ mA g}^{-1}$). The LFC–Na || NVP full cell surpassed the SP–Na || NVP and CS–Na || NVP cells in terms of maintaining capacity and recovering rates. In general, the higher the rate, the faster the charge and discharge speed, and the lower the ion conduction of the material, the capacity will be reduced.^[46] During cycling, the LFC Na full battery exhibits stable sodium deposition/stripping, as shown in the charge-discharge curves in Figure 6c. These tests demonstrate the LFC material's exceptional ion conductivity, which confirms the suitability of the LFC Na anode for the full battery.

3. Conclusions

In this study, utilizing lignin as the carbon source and magnesium oxide as the template agent results in carbon materials with abundant pore structures and a larger specific surface area. Moreover, due to the rich functional group structure in lignin, the prepared carbon material possesses a more diverse array of oxygen-containing functional groups compared to commercially available carbon materials. This

approach offers a promising strategy for tailoring carbon materials with enhanced properties, leveraging the unique characteristics of lignin as a renewable carbon precursor and magnesium oxide as a versatile template agent. The synthesized LFC material, investigated as a current collector for SMBs, A large specific surface area and excellent electrochemical performance are demonstrated. Analyses of SEM and in-situ optical microscopy show its effectiveness in inhibiting sodium dendrite growth. The LFC half-cell shows a low overpotential of -7 mV at 0.5 mA cm^{-2} . The symmetric battery based on LFC–Na exhibits a stable cycling for 400 hours at 0.5 mA cm^{-2} . Furthermore, the LFC–Na || NVP full battery delivers a capacity of 97.6 mAh g^{-1} at and maintains a capacity retention of 94.7% after 60 cycles. This research highlights the potential of LFC materials as promising candidates for advanced SMBs.

Acknowledgements

The authors acknowledge the financial support of the National Natural Science Foundation of China (22038004 and 22178069).

Conflict of Interests

The authors declare that they have no known competing financial interests or personal relationships that could have appeared to influence the work reported in this paper.

Data Availability Statement

The data that support the findings of this study are available on request from the corresponding author. The data are not publicly available due to privacy or ethical restrictions.

Keywords: lignin · three-dimensional current collector · porous carbon · sodium dendrite · sodium metal battery

- [1] X. T. Lian, N. Xu, Y. C. Ma, F. Hu, H. X. Wei, H. Y. Chen, Y. Z. Wu, L. L. Li, D. S. Li, S. J. Peng, *Chem. Eng. J.* **2021**, 421, 127755s.
- [2] S. J. Peng, L. L. Li, J. K. Y. Lee, L. L. Tian, M. Srinivasan, S. Adams, S. Ramakrishna, *Nano Energy* **2016**, 22, 361–395.

- [3] S. J. Peng, X. P. Han, L. L. Li, Z. Q. Zhu, F. Y. Cheng, M. Srinivansan, S. Adams, S. Ramakrishna, *Small* **2016**, *12*, 1359–1368.
- [4] P. Liu, H. T. Yi, S. Y. Zheng, Z. P. Li, K. J. Zhu, Z. Q. Sun, T. Jin, L. F. Jiao, *Adv. Energy Mater.* **2021**, *11*, 2101976.
- [5] H. J. Liu, M. Osenberg, L. Ni, A. Hilger, L. B. Chen, D. Zhou, K. Dong, T. Arlt, X. Y. Yao, X. G. Wang, I. Manke, F. Sun, *J. Energy Chem.* **2021**, *61*, 61–70.
- [6] D. Li, L. S. Cao, T. Deng, S. F. Liu, C. S. Wang, *Angew. Chem. Int. Ed.* **2021**, *60*, 13035–13041.
- [7] Z. W. Sun, Y. D. Ye, J. W. Zhu, E. Zhou, J. J. Xu, M. H. Liu, X. H. Kong, S. Jin, H. X. Ji, *Small* **2022**, *18*, 2107199.
- [8] L. L. Fan, X. F. Li, *Nano Energy* **2018**, *53*, 630–642.
- [9] N. W. Li, Y. X. Yin, C. P. Yang, Y. G. Guo, *Adv. Mater.* **2016**, *28*, 1853–1858.
- [10] C. L. Zhao, Y. X. Lu, J. M. Yue, D. Pan, Y. R. Qi, Y. S. Hu, L. Q. Chen, *J. Energy Chem.* **2018**, *27*, 1584–1596.
- [11] H. Wang, T. T. Jiang, B. Y. Wang, L. M. Zhang, D. Z. Kong, T. T. Xu, J. H. Zang, Z. F. Zhang, X. J. Li, Y. Wang, *J. Power Sources* **2021**, *507*, 230294.
- [12] Z. P. Li, K. J. Zhu, P. Liu, L. F. Jiao, *Adv. Energy Mater.* **2022**, *12*, 2100359.
- [13] B. Tang, Y. B. Zhao, Z. Y. Wang, S. W. Chen, Y. F. Wu, Y. Tseng, L. J. Li, Y. L. Guo, Z. Zhou, S. H. Bo, *eScience* **2021**, *1*, 194–202.
- [14] H. A. K. Toprakci, O. Toprakci, *Energies* **2023**, *16*, 16073169.
- [15] Z. Q. Zeng, X. Y. Jiang, R. Li, D. D. Yuan, X. P. Ai, H. X. Yang, Y. L. Cao, *Adv. Sci.* **2016**, *3*, 1600066.
- [16] W. Luo, C. F. Lin, O. Zhao, M. Noked, Y. Zhang, G. W. Rubloff, L. B. Hu, *Adv. Energy Mater.* **2017**, *7*, 1601526.
- [17] J. Ma, B. B. Chen, L. L. Wang, G. L. Cui, *J. Power Sources* **2018**, *392*, 94–115.
- [18] K. K. Li, J. Zhang, D. M. Lin, D. W. Wang, B. H. Li, W. Lv, S. Sun, Y. B. He, F. Y. Kang, Q. H. Yang, L. M. Zhou, T. Y. Zhang, *Nat. Commun.* **2019**, *10*, 09129.
- [19] E. Gabriel, C. R. Ma, K. Graff, A. Conrado, D. W. Hou, H. Xiong, *eScience* **2023**, *3*, 100139.
- [20] L. L. Mo, A. L. Chen, Y. Ouyang, W. Zong, Y. E. Miao, T. X. Liu, *ACS Appl. Mater. Interfaces* **2021**, *13*, 48634–48642.
- [21] F. Wu, J. H. Zhou, R. Luo, Y. X. Huang, Y. Mei, M. Xie, R. J. Chen, *Energy Storage Mater.* **2019**, *22*, 376–383.
- [22] S. F. Ye, L. F. Wang, F. F. Liu, P. C. Shi, Y. Yu, *eScience* **2021**, *1*, 75–82.
- [23] W. Luo, Y. Zhang, S. M. Xu, J. Q. Dai, E. Hitz, Y. J. Li, C. P. Yang, C. J. Chen, B. Y. Liu, L. B. Hu, *Nano Lett.* **2017**, *17*, 3792–3797.
- [24] Z. J. Zheng, X. X. Zeng, H. Ye, F. F. Cao, Z. B. Wang, *ACS Appl. Mater. Interfaces* **2018**, *10*, 30417–30425.
- [25] W. Yang, W. Yang, L. B. Dong, G. J. Shao, G. X. Wang, X. W. Peng, *Nano Energy* **2021**, *80*, 105563.
- [26] Z. Y. Fang, H. Y. Jiang, W. Qiu, Z. Y. Jiang, Z. W. Peng, K. Tian, C. H. Guan, M. Lu, M. S. Zhang, X. D. Li, *J. Phys. Chem. C* **2023**, *6*, 2835–2845.
- [27] Y. Y. Xie, J. X. Hu, Z. X. Han, T. S. Wang, J. Q. Zheng, L. Gan, Y. Q. Lai, Z. A. Zhang, *Energy Storage Mater.* **2020**, *30*, 1–8.
- [28] Z. L. Li, L. B. Deng, I. A. Kinloch, R. J. Young, *Prog. Mater. Sci.* **2023**, *135*, 101089.
- [29] R. Zhang, X. R. Chen, X. Chen, X. B. Cheng, X. Q. Zhang, C. Yan, Q. Zhang, *Angew. Chem. Int. Ed.* **2017**, *56*, 7764–7768.
- [30] A. Pei, G. Y. Zheng, F. F. Shi, Y. Z. Li, Y. Cui, *Nano Lett.* **2017**, *17*, 1132–1139.
- [31] R. Zhang, X. B. Cheng, C. Z. Zhao, H. J. Peng, J. L. Shi, J. Q. Huang, J. F. Wang, F. Wei, Q. Zhang, *Adv. Mater.* **2016**, *28*, 2155–2162.
- [32] K. N. Yin, D. Chen, C. S. Yin, Y. Zhong, X. L. Wang, J. P. Tu, *J. Electron. Mater.* **2023**, *52*, 5352–5361.
- [33] B. F. Tian, Z. X. Huang, X. L. Xu, X. H. Cao, H. Wang, T. T. Xu, D. Z. Kong, Z. F. Zhang, J. Xu, J. H. Zang, X. J. Li, Y. Wang, *J. Mater. Sci. Technol.* **2023**, *132*, 50–58.
- [34] X. Y. Zheng, P. Li, Z. Cao, W. Luo, F. Z. Sun, Z. Q. Wang, B. Ding, G. X. Wang, Y. H. Huang, *Small* **2019**, *15*, 1902688.
- [35] C. P. Yang, Y. G. Yao, S. M. He, H. Xie, E. Hitz, L. B. Hu, *Adv. Mater.* **2017**, *29*, 1702714.
- [36] N. Mubarak, F. Rehman, J. X. Wu, M. Ihsan-Ul-Haq, Y. Li, Y. H. Zhao, X. Shen, Z. T. Luo, B. L. Huang, J. K. Kim, *Nano Energy* **2021**, *86*, 106132.
- [37] Z. Tang, H. Wang, P. F. Wu, S. Y. Zhou, Y. C. Huang, R. Zhang, D. Sun, Y. G. Tang, H. Y. Wang, *Angew. Chem. Int. Ed.* **2022**, *61*, e202200475.
- [38] B. Sun, P. Li, J. Q. Zhang, D. Wang, P. Munroe, C. Y. Wang, P. H. L. Notten, G. X. Wang, *Adv. Mater.* **2018**, *30*, 1801334.
- [39] N. Mubarak, F. Rehman, M. Ihsan-Ul-Haq, M. Y. Xu, Y. Li, Y. H. Zhao, Z. T. Luo, B. L. Huang, J. K. Kim, *Adv. Energy Mater.* **2022**, *12*, 2103904.
- [40] Y. P. Zhuang, D. Y. Deng, L. Lin, B. Liu, S. S. Qu, S. C. Li, Y. G. Zhang, B. S. Sa, L. S. Wang, Q. L. Wei, L. Q. Mai, D. L. Peng, Q. S. Xie, *Nano Energy* **2022**, *97*, 107202.
- [41] Q. Z. Jin, H. F. Lu, Z. L. Zhang, J. Xu, B. Sun, Y. Jin, K. Jiang, *Adv. Sci.* **2022**, *9*, 2103845.
- [42] H. Shi, Y. M. Zhang, Y. Liu, C. Z. Yuan, *Chem. Rec.* **2022**, *22*, e202200112.
- [43] L. Geng, C. Zhao, J. T. Yan, C. R. Fu, X. D. Zhang, J. M. Yao, H. M. Sun, Y. Su, Q. N. Liu, L. Q. Zhang, Y. F. Tang, F. Ding, J. Y. Huang, *J. Mater. Chem. A* **2022**, *10*, 14875–14883.
- [44] G. Wang, X. H. Xiong, P. J. Zou, X. X. Fu, Z. H. Lin, Y. P. Li, Y. Z. Liu, C. H. Yang, M. L. Liu, *Chem. Eng. J.* **2019**, *378*, 122243.
- [45] Z. H. Li, K. Liu, K. Fan, Y. S. Yang, M. F. Shao, M. Wei, X. Duan, *Angew. Chem. Int. Ed.* **2019**, *58*, 3962–3966.
- [46] J. X. Wu, P. C. Zou, M. Ihsan-Ul-Haq, N. Mubarak, A. Susca, B. H. Li, F. Ciucci, J. K. Kim, *Small* **2022**, *16*, 2003815.

Manuscript received: January 24, 2024

Revised manuscript received: February 23, 2024

Accepted manuscript online: March 1, 2024

Version of record online: March 15, 2024